# Spatial and temporal variations of seismic azimuthal anisotropy following the 2019 ridgecrest earthquake sequence in southern california

Yan Jia [a,b], Stephen S. Gao [b], Kelly H. Liu [b,*]

[a] *Key Laboratory of Submarine Geosciences, Second Institute of Oceanography, Ministry of Natural Resources, Hangzhou 310012, China*
[b] *Department of Earth Sciences and Engineering, Missouri University of Science and Technology, Rolla, MO 65409, USA*

## ARTICLE INFO

## ABSTRACT

To investigate the spatial and temporal variations of seismic azimuthal anisotropy in the vicinity of the conjugate fault network activated by the 4 July 2019 (UTC) M6.4 foreshock and the 6 July 2019 M7.1 mainshock in Ridgecrest, California, a total of 1,470 shear wave splitting measurements were obtained from local events recorded by five seismic stations over the period of July 2019 to January 2020. The results suggest a strong asymmetry in anisotropy forming mechanisms across the NW-SE striking Eastern Little Lake Fault, which is the main fault of the area. In the area located to the northeast of the main fault, the observed fast orientations are dominantly N-S, which is parallel to the maximum horizontal compressive stress. In the area surrounding the main fault, the fast orientations are primarily parallel to the strikes of multiple fault zones including the main fault and the crossing faults, rather than solely consistent with that of the main fault, which may indicate along-strike variations in fault strength of the main fault. To the southwest of the main fault, the observed anisotropy is jointly controlled by faults or regional stress. The observed NE-SW-oriented anisotropy in the vicinity of two previously proposed blind faults confirms the existence of faults. The splitting times of anisotropic areas with different inducements are independent of the focal depths, suggesting that either the stress- or structure-induced anisotropy is mostly located in a shallow layer in the top several kilometers. A nearly 90-degree switch in the fast orientations and greatly reduced splitting times from a group of nearby earthquakes may indicate fault zone healing.

## 1. Introduction

The July 2019 Ridgecrest, California earthquake sequence, consisting primarily of an M6.4 foreshock on 4 July (UTC), an M7.1 mainshock on 6 July, and tens of thousands of recorded aftershocks, activated a complex network of intertwined conjugate faults in the southern Walker Lane (Fig. 1) (e.g., Barnhart et al., 2019; Ross et al., 2019; DuRoss et al., 2020; Fielding et al., 2020; Hauksson et al., 2020; Ponti et al., 2020; Shelly, 2020). The activated fault network mainly includes the NW-SE striking Eastern Little Lake Fault (ELLF) and the NE-SW striking Southern Little Lake Fault (SLLF) and several other faults (Fig. 1b) (Hauksson et al., 2020; Plesch et al., 2020). In addition to the surface ruptures, Shelly (2020) and Plesch et al. (2020) reported several possible NE-SW blind faults that are approximately normal to the middle-south segment of the ELLF. The southern aftershock zone of the 2019 Ridgecrest M7.1 earthquake almost contains the entire concentration of these conjugate fault systems. A detailed description of the distribution of the

fault system can be found in Fig. S1. The averaged maximum horizontal compressive stress (SHmax) direction obtained from focal mechanism inversions in the Ridgecrest area is nearly N-S, and a rotation of a few degrees after the mainshock has been proposed (Fig. 1; Sheng and Meng, 2020; Duan et al., 2022).

Although numerous studies have been conducted after the 2019 Ridgecrest earthquake sequence to understand surface deformation and stress field distribution and evolution (e.g., Ross et al., 2019; DuRoss et al., 2020; Fielding et al., 2020; Shelly, 2020; Sheng and Meng, 2020; Fialko and Jin, 2021; Yue et al., 2021; Duan et al., 2022), one important type of measurements that is still missing is the spatial and possible temporal variations of azimuthal anisotropy in the seismogenic zone. While GPS and remote sensing-based techniques map the deformation field at the surface and focal mechanism solutions provide insights into the stress regime in the fault zones, seismic anisotropy measurements, like those presented below, have the potential to provide critical information about the deformation field in the seismogenic zone (e.g.,

Crampin, 1978; Cochran et al., 2003; Boness and Zoback, 2004; Z. Li et al., 2014; T. Li et al., 2019; Shi et al., 2020; Y. Liu et al., 2021). By measuring seismic azimuthal anisotropy, one can decipher the lateral and vertical distribution, as well as orientation and temporal variations of seismogenic layer fractures that are associated with fault zones and fluid-filled micro-fractures formed in response to regional compressive stress.

### 1.1. Shear wave splitting analysis and seismogenic layer azimuthal anisotropy

Shear wave splitting (SWS) analysis is one of the most frequently employed techniques to map azimuthal anisotropy along the ray paths (Crampin, 1991, 1994; Miller and Savage, 2001; Peng and Ben-Zion, 2004; Y. Liu et al., 2008). The linearly polarized shear wave splits into two nearly perpendicular quasi-shear waves with different speeds when it propagates through an anisotropic medium (Ando, 1980; Silver and Chan, 1991). The polarization orientation of the fast wave (fast orientation or ϕ) and the time of separation between the fast and slow waves (splitting time or δt) are unambiguous indicators of the orientation and strength of azimuthal anisotropy, respectively.

Azimuthal anisotropy developed in the brittle upper continental crust is typically attributed to localized tectonic stress-controlled, fluid-filled, microcracks and is mostly parallel to the SHmax orientation. Anisotropy thus formed is termed stress-induced anisotropy (Crampin, 1978; Leary et al., 1990; Boness and Zoback, 2004). Anisotropy can also be associated with geological structures (Boness and Zoback, 2006) with an orientation that is consistent with the dominant strike of fracture

zones such as those associated with active faults, i.e., structure-induced anisotropy (Zhang and Schwart, 1994; Zinke and Zoback, 2000; Z. Li and Peng, 2017). Moreover, other mechanisms such as magmatic dikes and oriented melt pockets (S. Gao et al., 1997; Keir et al., 2005; Bastow et al., 2010), preferential mineral alignment (Brocher and Christensen, 1990; Sayers, 1994) and sedimentary layering (Leary et al., 1990; Bastow et al., 2010; Audet, 2015) can also cause crustal anisotropy.

### 1.2. Rationale of the study

This study represents the first SWS analysis focused on the southern aftershock zone of the 2019 Ridgecrest earthquake sequence, where conjugate faults are clearly identified (Shelly, 2020; Plesch et al., 2020; Fialko and Jin, 2021). We mostly rely on individual rather than station- or area-averaged SWS measurements to identify spatially varying anisotropy in the seismogenic layer, allowing us to conduct a detailed investigation of the spatial distribution in upper crustal anisotropy. We also attempt to explore possible temporal variations of anisotropy, which may reflect rock property changes as a result of fluid injection (e. g., Miller and Savage, 2001; Volti and Crampin, 2003; T. Li et al., 2019), perturbation of the local stress field (e.g., Y. Gao and Crampin, 2004), changes in rock and static stress physical properties related to large earthquakes (e.g., Crampin, 1994; Y. Liu et al., 1997; Y. Gao et al., 1998), and fault zone healing processes after a major earthquake (e.g., Tadokoro and Ando, 2002; Hiramatsu et al., 2005). Seismic events with almost identical ray paths are employed in this study to remove spatial effects (e.g., Aster et al., 1990; Bokelmann and Harjes, 2000; Y. Liu et al., 2004; Peng and Ben-Zion, 2004) to explore possible fault healing
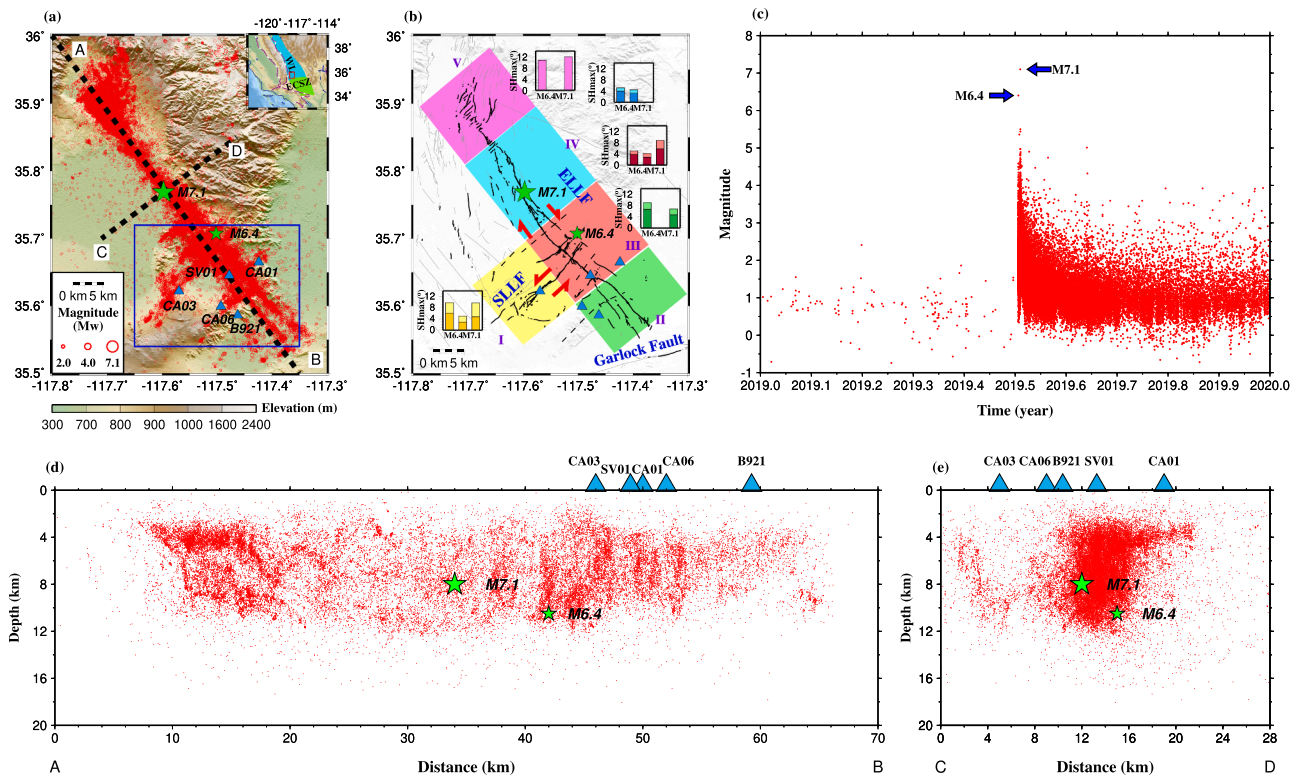


**Fig. 1.** (a) Distribution of seismic stations used in the study (light-blue triangles) and earthquakes that occurred in 2019 (red dots). The green stars show the epicenters of the M6.4 (4 July 2019), and M7.1 (6 July 2019) earthquakes. The study area is marked by the blue rectangle. The inset map in the upper-right corner shows the location of the main map. WL: Walker Lane; ECSZ: Eastern California Shear Zone. (b) Fault network in the 2019 Ridgecrest aftershock zone. The grey, black solid, and black dashed lines indicate the Quaternary faults (Wills, 1988; see Data Availability Statement), the surface ruptures (DuRoss et al., 2020; Ponti et al., 2020), and the blind faults (Hauksson et al., 2020; Plesch et al., 2020) formed after the M7.1 Ridgecrest earthquake sequence, respectively. The colored polygons and histograms show the distribution and variations of the orientation of the maximum horizontal compressive stress (SHmax) in different subzones (I–V) of the mapped area (lighter colors: Sheng and Meng, 2020; darker colors: Duan et al., 2022). In each of the histograms, the columns from left to right represent the SHmax in the time-period prior to the M6.4 foreshock, between the M6.4 and M7.1 earthquakes, and after the M7.1 mainshock, respectively. (c) A plot of earthquake magnitudes against origin times. (d) Distribution of earthquakes projected to Profile A–B in (a). (e) Distribution of earthquakes projected to Profile C–D in (a).

following the M7.1 Ridgecrest earthquake.

## 2. Data and methods

The seismic dataset used in this study was recorded by five stations, which including four temporary stations (CA01, CA03, CA06, and SV01) and one permanent station (B921) located in the conjugate fault network in the southern aftershock zone of the 2019 Ridgecrest earthquake sequence (Figs. 1a, 1b and S1b). Data collected by the three CA stations and Station B921 were obtained from the Seismological Facility for the Advancement of Geoscience (SAGE) Data Management Center (DMC), and those collected by Station SV01 were obtained from the Southern California Earthquake Data Center (SCEDC) (Fig. 1a). The four temporary stations were deployed by the U.S. Geological Survey (USGS; Cochran et al., 2020) following the M6.4 foreshock and M7.1 mainshock. The earliest earthquake obtained by Station B921 was in late April 2019, while the other four stations collected data with a recording length of about 4–6 months, from early July 2019 until January 2020. A total of 37,584 earthquakes were reported in the mapped area of Fig. 1 during 2019 and were relocated by the SCEDC (https://scedc.caltech.edu/; Fig. 1). For data requests, we apply a minimum cutoff magnitude of −0.74, which is the minimum magnitude in the catalog, to ensure that all recorded seismic events can be utilized. According to a previous P- and S-wave velocity tomography study in the local area, the Vp/Vs value at ~17 km near the bottom of the brittle upper crust is about 1.80 (White et al., 2021). Therefore, only events with an angle of incidence of less than 33.75° (computed using $asin(Vs/Vp)$) are used for SWS analysis in this study, to avoid the distortion of particle motions of the direct S-wave by the free surface (e.g., Nuttli, 1961; Booth and Crampin, 1985).

Using a semi-automatic procedure (K.H. Liu et al., 2008; Liu and Gao, 2013) developed based on the principle of minimizing the lesser of two eigenvalues of the covariance matrix (Silver and Chan, 1991), we simultaneously search for the initial polarization direction and the optimal pairs of splitting parameters (including the fast orientation and splitting time). Once the initial polarization direction and the splitting parameters are found, the horizontal seismograms are rotated to the initial polarization parallel (P$_{//}$) and initial polarization perpendicular (P⊥) components. The corrected P$_{//}$ and P⊥ components, the fast and slow components, the particle motion patterns, and the remaining energy on the corrected P⊥ components are then computed, in the same manner as the minimization of transverse energy approach (Silver and Chan, 1991), for visual display and manual checking. The *F*-test approach specified in Silver and Chan (1991) is employed to estimate the uncertainties in the individual measurements, which are expressed as one standard deviation. The original seismograms are initially bandpass filtered with corner frequencies of 0.5 and 10.0 Hz, while the S-phase signal-to-noise ratio (S/N) of the P$_{//}$ components of retained seismic events should exceed 3.0 after filtering. The initial setting for the beginning and ending times of the direct S window is $T_s$-0.2 s and $T_s$+0.5 s, respectively, where $T_s$ represents the calculated theoretical arrival times of the direct S phase using the IASP91 Earth model (Kennett and Engdahl, 1991). This global velocity model is only used to estimate the approximate arrival time of direct S waves and may lead to a maximum error of about 0.3 s if a local velocity model (White et al., 2021) is used. As mentioned in the following paragraph, the initially set time windows are manually checked and adjusted if necessary, and therefore, this error does not affect the results.

All the resulting measurements are then automatically ranked following the criterion which was referred in K.H. Liu et al. (2008) and subsequently visually verified and classified into four ranks as A (outstanding; for those exhibiting robust direct S arrivals on both the original P$_{//}$ and P⊥ components, with effectively removed energy on the corrected P⊥ components, and demonstrating a notable linearity in the corrected particle motions), B (good; similar to rank A measurements but with lower S/N on the P$_{//}$ component, and acceptable but weaker

linearity of the corrected particle motions), C (unusable; for those displaying no clear direct S arrival on the original P$_{//}$ and P⊥ components, or poor linearity of the corrected particle motion), and N (null; for those the direct S energy is only observed on the P$_{//}$ component but not on the P⊥ component). If necessary, the beginning and end of the window for SWS analysis and the band-pass filtering frequencies are modified during the manual checking stage to exclude non-S arrivals and improve the S/N. After the splitting results become stable with different time window selections (Figs. S2 and S3), the final ranking of the measurements is determined based on the quality of the signal, the linearity of the corrected particle motions, and the uniqueness and strength of the minimum energy point on the misfit map of the corrected P⊥ component. Some of the measurements have two possible pairs of splitting parameters (e.g., Figs. S4 and S5) and might be related to cycle skipping, as discussed in the Supporting Information. Only measurements with quality A or B are used on the following interpretations. Examples of splitting analysis from the five stations used in the study are shown in Figs. S6–S10.

## 3. Results

After manual checking, a total of 1470 pairs of well-defined (Rank A or B) splitting parameters are obtained, among which 236 are from Station CA01, 204 from Station CA03, 280 from Station CA06, 425 from Station B921, and 325 from Station SV01. The splitting parameters from each of the five stations plotted at the epicenters and the middle points between the events and the stations can be found in Figs. 2 (for Station CA03) and S11–S14 (for the rest of the stations). The regional SHmax orientation used in the following analysis is 5.1°, representing the arithmetic mean value of SHmax obtained based on the stress inversion results from the focal mechanism solutions following the occurrence of the M7.1 mainshock for subzones I–III (Duan et al., 2022) (Fig. 1). Table S1 contains the splitting parameters and related event information for all 1470 measurements, and Table S2 shows station-averaged splitting parameters (Note: plots similar to Figs. S6–S10 for all the 1470 measurements can be found at https://github.com/yj5mc/RC_SWS_measus.git). The magnitudes of related events range from 0.1 to 4.1. For all the measurements, the circular mean of the fast orientations is 32.7 ± 30.6°, the arithmetic mean of the delay times is 0.06 ± 0.03 s, and the mean ray-path-length normalized splitting time (NST) is 7.36 ± 4.19 ms/km. The mean and median values of the standard deviations of the individual measurements (Table S1) are 7.9° and 6.5° for the fast orientation and 0.0077 s and 0.01 s for the splitting time, respectively. Note that the standard deviations could be underestimated due to the fact that the method of Silver and Chan overestimated the degrees of freedom (Walsh et al., 2013). Fig. 3 shows the spatial distribution of the resulting fast orientations, and Fig. 4 shows that of the splitting times.

When plotted at the epicenters, the splitting parameters of seismic events in the same region obtained by different seismic stations are obviously different (Fig. 3). Specifically, the measurements obtained from Station CA01 (red bars in Fig. 3a) are mainly distributed to the north of the ELLF, whose ray paths hardly cross the ELLF. These measurements exhibit dominantly N-S fast orientations, which are consistent with the SHmax orientation. As for Station SV01 (purple bars in Fig. 3a), the observed fast orientations are mainly ENE-WSW, which are between the NW-SE strike of the ELLF and the NE-SW strike of the cross faults. The epicenters of a portion of seismic events from Station SV01 overlapped with those from Station CA01, but the fast orientations of the splitting parameters obtained at the two stations are apparently different. Measurements obtained by Stations CA06 (blue bars in Fig. 3a) and B921 (light brown bars in Fig. 3a) are mainly from the vicinity of the multiple cross faults including the Cross-South-South blind fault. Most of the measurements of Station CA06 are located between the ELLF and the Cross-South-South blind fault and show apparent spatial variation. The fast orientations obtained at Station CA06 from events near the Cross-South-South blind are NE-SW, which are parallel to the blind fault,
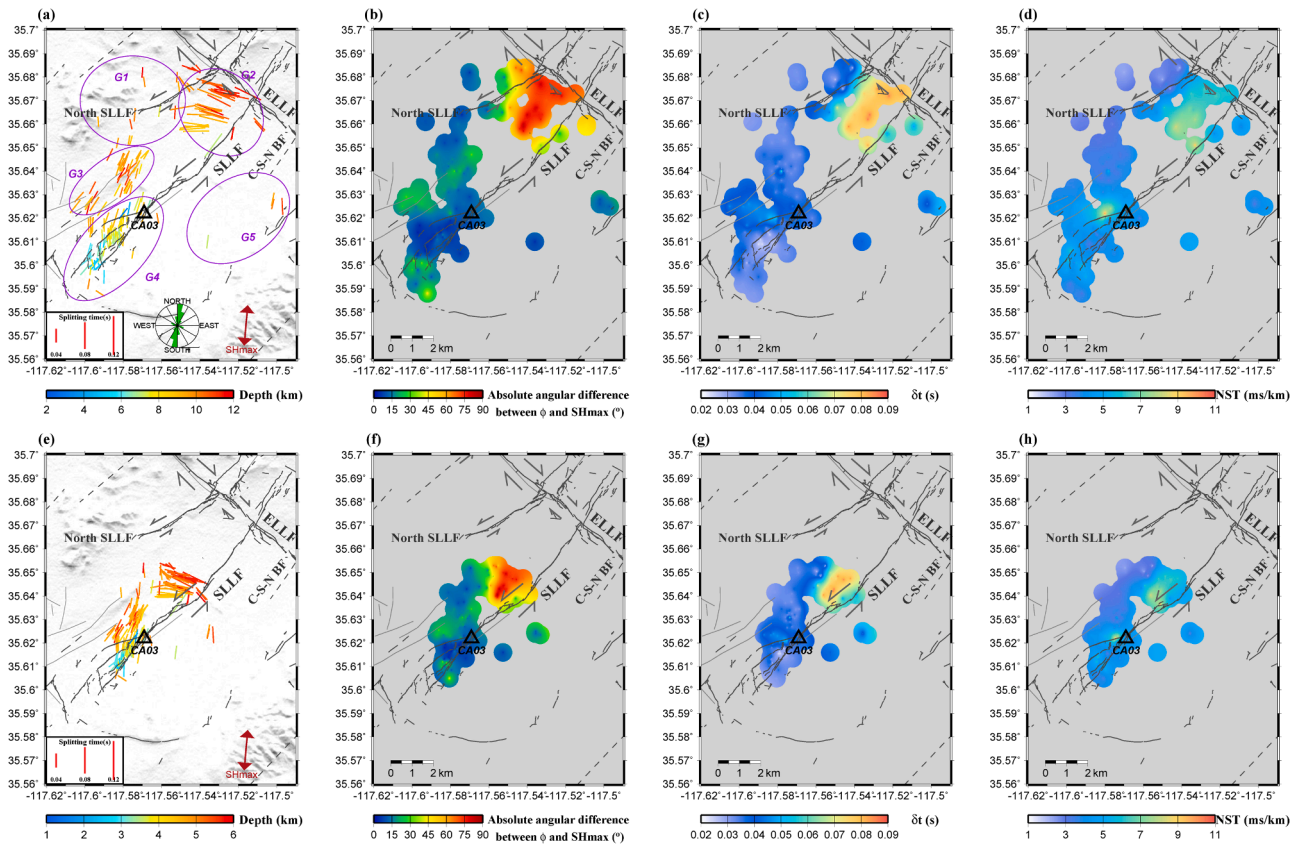
**Fig. 2.** (a) Resulting SWS parameters of Station CA03 plotted at the epicenters. The color of the bars indicates focal depths. (b) Absolute angular difference between fast orientations and SHmax orientation (Duan et al., 2022). (c) Resulting splitting times. (d) Ray path normalized splitting times. (e–h) Same as (a–d) but for measurements plotted at the middle of ray paths between the epicenters of events and stations. C-S-N BF: Cross-South-North blind fault; North SLLF: north branch of the SLLF. Dark red double-sided arrow in the lower right corner of (a) and (e) indicates the regional average SHmax orientation, which is 5.1° (Duan et al., 2022). To produce the images shown in (b–d) and (f–h), the data is firstly fitted using an adjustable tension continuous curvature surface gridding algorithm (Smith and Wessel, 1990), and then all the areas having a distance greater than 0.005° from the nearest data point are covered in grey.

while the fast orientations gradually shift to the non-fault parallel N-S orientations for events obtained at Station CA06 near the main ELLF. In contrast, no matter whether the ray path traverses the Cross-South-South blind fault, the fast orientations from Station B921 (light brown bars in Fig. 3a) show consistent NE-SW fast orientations.

In the area south of the ELLF and west of the SLLF, the observed measurements are almost exclusively from Station CA03 (green bars in Fig. 3a). According to the distribution of seismic events and their corresponding splitting parameters' characteristics, measurements from this station can be divided into five groups (Fig. 2). Groups 1 and 5 are located on the west and east sides of the SLLF, respectively, and the fast orientations are parallel to the SHmax orientation. However, the fast orientations of the splitting parameters in Group 2, which is situated in the conjugate fault zone between the SLLF, the ELLF, and the North SLLF, exhibit a significant parallelism with the NW-SE strike of the ELLF. The events of Group 3 predominantly occurred from several Quaternary faults (Wills, 1988), which mainly exhibit NNE-SSW fast orientations that are roughly parallel to the Quaternary faults. Group 4 primarily consists of measurements from seismic events occurring on the fault branches in the southwest section of the SLLF, most of which have a fast orientation that aligns with the SHmax orientation.

The distinct spatial variations are manifested through the differential splitting times of the measurements obtained from the five seismic stations (Fig. 4). Specifically, the smallest splitting times in the entire study area are concentrated around the north of the ELLF, as observed by Station CA01, and the north of the SLLF, as observed by Station CA03. Greater splitting times are observed around the ELLF and to the northwest of the Cross-South-South blind fault. Significant increases in NST

values compared to the surrounding area are particularly notable from events in the conjugate fault zone between the ELLF, the SLLF, and the North SLLF. In addition, both sides of the Cross-South-South blind fault and the area to the north of the intersection of the Short-Cross-Sinistral-Rupture and the ELLF also show greater NST values. Detailed analyses of the spatial distribution of the splitting parameters obtained by each of the stations can be found in the Supporting Information section.

## 4. Discussion

When the measurements are interpreted, it is important to realize that the observed anisotropy is accumulated along the entire ray path in spite of the fact that they are displayed at the epicenters or at the middle of the ray paths in Figs. 3,4 and S11–S14. The ray path samples a "banana" shaped Fresnel zone with a size that is dependent on the frequencies and distance to the station. For instance, the radius of the first Fresnel zone for a 7 Hz S-wave is about 1 km at a distance of 5 km from the station. If the upper crust anisotropy is induced by regional stress, it accumulates uniformly along the ray path. On the other hand, in areas with dominantly structure-induced anisotropy, it is reasonable to assume that the anisotropy may not be uniformly distributed along the entire ray path but is mainly concentrated near the earthquake foci. As shown in Fig. S15, the standard deviation (STD) of spatially averaged fast orientations is apparently reduced if we plot the measurements at the middle of the ray paths instead of the epicenters of events.

In the following we project the measurements at the middle of the ray paths and divide the study region into nine areas (Areas A – I; Fig. 5 and S16). Area A includes the area northeast away from the ELLF and

**Fig. 3.** Spatial distribution of the SWS measurements from all five stations plotted at the epicenters of events. (a) The orientation of the bars represents the fast orientation, and the length is proportional to the splitting time. The red, green, blue, light brown, and purple bars represent the measurements from Stations CA01, CA03, CA06, B921, and SV01, respectively, and the rose diagrams are created using all the fast orientation measurements from associated stations. Measurements from Station CA06 in the black circle near the center of the diagram show temporal variations. Dark red double-sided arrow in the lower right corner indicates the regional average SHmax orientation of 5.1° (Duan et al., 2022). (b) Absolute angular difference between fast orientations and the SHmax orientation. (c) The zoom-in map showing the temporal variation of splitting parameters observed in the black circle in (a). Lines with burlywood color indicate the ray paths between the Station CA06 and measurements. S-C-S-R: Short-Cross-Sinistral-Rupture.

southeast of the Cross-South-North blind fault, and the measurements are all from Station CA01 plus one from Station SV01. Area B includes the other SV01 measurements and is located southeast of the SLLF surrounding the ELLF and the Cross-South-North blind fault. Areas C, D, E, F, and G contain the measurements from Groups 1–5 of Station CA03, respectively (Fig. 2). Area H contains the measurements located southwest of the ELLF and southeast of the SLLF, mainly from Station CA06 and, to a lesser extent, from Station B921. Area I includes the area in the

vicinity and southeast of the Cross-South-South blind fault, and the measurements are mostly from Station B921 plus a few from CA06. The averaged results of measurements for each of the areas can be found in Table S3.

### 4.1. Regional stress induced anisotropy (Areas A, D, F, and G)

The fast orientations of anisotropy in Areas A, D, F, and G are

**Fig. 4.** (a) Resulting splitting times plotted at the epicenters. (b) Ray-path-length normalized splitting time.
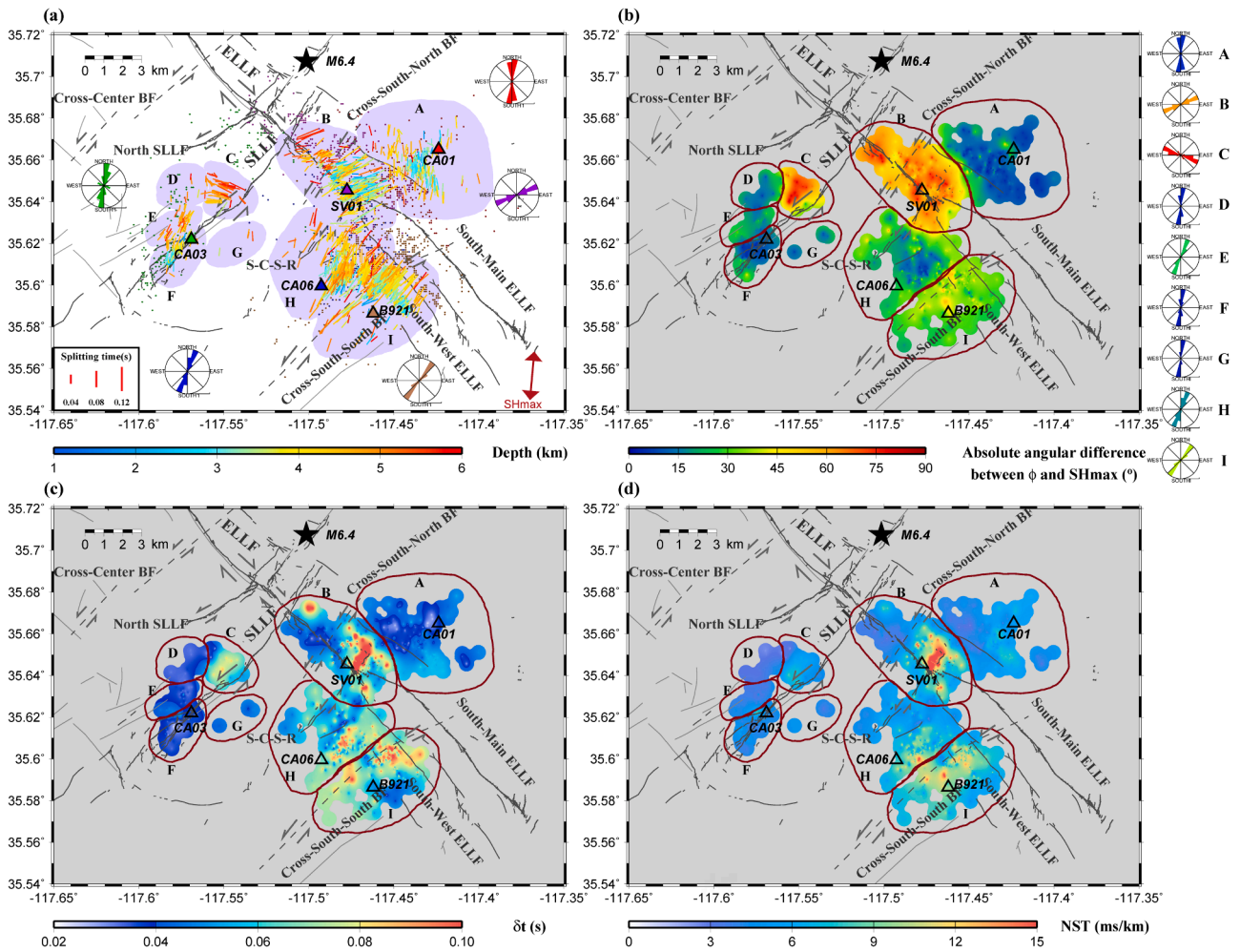
**Fig. 5.** Spatial distribution of the SWS measurements from all five stations plotted at the middle of ray paths. (a) Resulting individual SWS parameters. The color of the bars indicates focal depths. Measurements with different colors in the rose diagrams are obtained from the corresponding stations (triangles) plotted using the same color. Dark red double-sided arrow in the lower right corner indicates the regional average SHmax orientation of 5.1° (Duan et al., 2022). (b) Absolute angular difference between fast orientations and SHmax orientation. (c) Resulting splitting times. (d) Ray path normalized splitting times. The entire study area is divided into nine subareas according to the fast orientations of the splitting parameters (Fig. S16b). Different areas are marked by the light purple shades (a) or dark red polygons (b–d).

dominantly N-S, i.e., SHmax parallel (Fig. 5b), with no systematic spatial variations. These four subareas exhibit the weakest anisotropy in the entire study area with the smallest splitting times and NST values (Figs. 5c and 5d). The related anisotropy can be attributable to the regional stress field and is accumulated along the ray paths. The faults through which the ray paths of these events pass, for example, the end of the North SLLF and the southwest end of the SLLF and the South-Main ELLF, are significantly less developed, as indicated by the lack of fault parallel anisotropy. The match between the two orientations is reduced for measurements from events in the southwestern horsetail termination of the SLLF in Area F and may reflect the partial influence of fault zone anisotropy.

Although the focal depths vary considerably in the four areas (Fig. 5a), the splitting times are largely independent of the focal depths (Fig. S17a–d), suggesting that regional stress induced anisotropy is concentrated at shallow depths, probably above ~5 km, which is the focal depths for most of the shallowest events. The largest splitting times in the four areas are observed from events in the southwestern part of Area A, about 1.5 km from the South-Main ELLF (Fig. 5c). A possible cause of the large splitting times in this area is reduced rock strength associated with the intensive deformation in the fault zone, leading to more developed SHmax-parallel micro-fractures.

### 4.2. Anisotropy associated with surface and blind faults (Areas B, C, E, H and I)

Previous upper crustal anisotropy studies generally suggested that areas near fault zones normally exhibit more complex anisotropy, making it difficult to determine possible origin (e.g., Baccheschi et al., 2016; Shi et al., 2020). In a complex fault system such as our study area, we speculate that anisotropic orientation departure may reflect contributions from multiple local fault structures and the regional stress field. Although similar mixed mechanisms have been mentioned in several previous studies, the related study areas are mostly either located in extensional regimes where the main active fault strike is almost consistent with SHmax orientation (e.g., Pastori et al., 2019), or one of multiple observed anisotropy has significantly greater strength (e.g., Jiang et al., 2021), only the partial accumulations or cancellations of anisotropy strength without significant variations in the anisotropic orientation were reported.

In our study, the fast orientations from events in Areas C and I are largely parallel to the strikes of known faults or previously proposed blind faults (Fig. 5), suggesting fractures in the individual fault zones are mostly responsible for the observed anisotropy. The resulting fast orientations of anisotropy observed in Areas B, E, and H are more or less oriented to the direction in between the strikes of the nearby faults and

the SHmax, probably indicating joint contributions from stress- and structure-induced anisotropy. The lack of a positive correlation between the focal depths and the splitting times in the areas associated with stress-induced and fault-induced anisotropy indicates that both types of anisotropy should be concentrated at a shallow depth, approximately in the top several kilometers (Fig. S17).

Area B is located in the middle section of the ELLF, where the main segment of the ELLF intersects with NE-SW-oriented and NW-SE-oriented faults (Fig. 5). In the region north of the intersection of ELLF and Short-Cross-Sinistral-Rupture, a NE-SW oriented linear zone of approximately 2 km in length and 1 km in width with the strongest anisotropic strength in the entire study area was observed (Figs. 5c and 5d). The strong anisotropy north of the ELLF may indicate the length of the Short-Cross-Sinistral-Rupture is longer than proposed. The greater splitting times observed north of the ELLF relative to the southern area is consistent with the asymmetry in the distribution of earthquakes (Fig. S18), i.e., the number of earthquakes near the Short-Cross-Sinistral Rupture south of the ELLF is significantly lower than that in the north, which may indicate an asymmetry in fracture strength and density between the north and south sides of the ELLF. Additionally, the fast orientations in this area are spatially varying with ENE-WSW orientations. The observed anisotropy close to the E-W orientation suggests that the influences of the ELLF and NE-SW-oriented cross faults are comparable, while the anisotropy aligned with the NE-SW orientation reveals the greater contribution of the cross faults.

Anisotropy in Area C demonstrates one of the clearest parallelisms between the fast orientations and the fault strike (Fig. 5a). The observed NW-SE fast orientations and relatively larger splitting times are determined through measurements of events with epicenters situated within the ELLF section between the SLLF and the North SLLF (Fig. 2). The fault-parallel fast orientations are still observable for events located ~2 km away from the surface expression of the ELLF. Approximately 3 km away from the ELLF, the fast orientations shift towards an E-W direction, indicating a weakening of the anisotropy strength controlled by the ELLF and a transition to the joint control of the ELLF and SLLF. In contrast, less ELLF-parallel anisotropy is observed in the section of the ELLF southeast of the SLLF, which is consistent with the sharp reduction in the diffusively distributed earthquakes along the ELLF (Fig. S18).

The combined contribution of N-S-oriented regional stress and the presence of NE-SW-oriented well-developed along-strike fractures associated with the SLLF and nearby reactivated Quaternary faults can satisfactorily explain the NNE-SSW fast orientations in Area E. Areas H and I are distributed in the north and south side of the Cross-South-South blind fault, respectively. In Areas H and I, strong NE-SW oriented anisotropy for events in the vicinity of two proposed NE-SW blind faults (the Cross-South-South and Cross-South-North blind faults), which is consistent with the area of significant velocity contrast across the blind faults reported by White et al. (2021), is observed. It is noticed that the anisotropy in the vicinity of and to the south of the Cross-South-South blind fault is parallel to the blind fault, while the anisotropy to the north of the blind fault exhibits a rotation from NE-SW to N-S with the decreased distance to the South-West ELLF. A possible interpretation is that the main segment of the ELLF and the South-West ELLF developed an extensional duplex structure around the South-West ELLF, forming roughly N-S oriented tensile ruptures (Woodcock and Fischer, 1986).

### 4.3. Asymmetry in rock strength across the ELLF

One of the most intriguing features in the observed seismogenic zone anisotropy pattern is that the ELLF serves as a boundary between two regions of different anisotropic formation mechanisms. The observed anisotropy (Area A) from events located ~1.5 km or further away to the northeast of the ELLF is dominated by N-S fast orientations that are most likely formed by regional compressional stress. Fast orientations observed in the area within and to the southwest of the fault are generally dominantly or partially fault-controlled (Fig. 5a). Such a

contrast may suggest that the area to the northeast of the ELLF is less fractured by the strike-slip fault system, probably due to a relatively stronger seismogenic zone. This is consistent with the observation that most of the NE-SW oriented faults are located in the area to the south-west of the ELLF or extend a short distance across it.

### 4.4. Possible temporal variations of the observed anisotropy

Temporal variations in the strength and orientation of upper crustal anisotropy may reflect regional stress changes or significant tectonic movements related to coseismic or postseismic processes (e.g., Crampin, 1994; Y. Liu et al., 1997; Tadokoro and Ando, 2002; Y. Gao and Crampin, 2004). For instance, a set of 7 measurements at Station CA06 from seismic events located in the intersection area of the ELLF and the Cross-South-North blind fault (the black circle in Figs. 3a, 3c and S12a) exhibits clear temporal variations in both the fast orientation and splitting time (Fig. 6). As shown in Figs. 3 and S19, for the four events that occurred between 3 August and 21 August (days 215–233) in 2019, the fast orientations are orthogonal to the ELLF and the splitting times are 0.09–0.10 s, which are among the largest in the study area (Figs. 6a–6d). In contrast, the fast orientations from the three events between 26 October and 25 November (days 299–329) changed to parallel to the strike of the ELLF, and the splitting times reduced to 0.03 s (Figs. 6e–6g). The observed splitting parameters in the same group are almost identical to each other, including the focal mechanisms and the estimated initial-S wave polarization directions. Note that this high level of similarity, together with the fact that the foci of the events are less than 1 km (~0.75 km) from each other, resulted in an apparently reduced number of measurements (from 7 to 3) in Figs. 3c and S11a.

The ray paths of the seven measurements traverse a group of NE-SW oriented conjugate faults and perhaps also the NW-SE oriented shear zone of the ELLF (Figs. 3c and S12a). Therefore, the NE-SW fast orientations observed in the earlier group of events may indicate the existence of fractures associated with the conjugate fault system that were probably developed or reactivated by the M7.1 earthquake sequence (Shelly, 2020). The fact that the fast orientations changed to ELLF parallel in the later group may suggest healing of the NE-SW oriented fractures that should occur between 21 August and 26 October, as observed elsewhere (e.g., Tadokoro and Ando, 2002; Hiramatsu et al., 2005), and anisotropy associated with the ELLF became dominant along this particular ray path. Unfortunately, due to the gap between the occurrence of the two groups of measurements, no gradual variations in splitting parameters were observed (Fig. S19), making it difficult to discuss the time scale of the healing process.

### 5. Conclusions

Based on 1470 pairs of splitting parameters observed by five stations in the southern 2019 Ridgecrest aftershock zone, systematic spatial variations in the orientation and formation mechanisms of azimuthal anisotropy in seismogenic zone beneath the complicated conjugate fault network are revealed. Anisotropy in the area to the northeast of the ELLF is mostly N-S oriented and is the result of regional compressive stress, and that surrounding the ELLF is dominated by shear zones associated with two groups of intersecting active faults. To the southwest of the ELLF, anisotropy is primarily governed by the mixture of cross faults and regional stress fields. Two hypothesized cross-blind faults are confirmed to exist in the observed area with the highest consistency with the strike of fractures. The different anisotropy forming mechanisms imply an asymmetry of rock strength across the ELLF. The northern section of the ELLF and the Cross-South-South blind fault in the study area demonstrate the strongest fault-parallel anisotropy, followed by the SLLF and Cross-South-North blind faults. Almost no NW-SE oriented fault-parallel anisotropy is observed from events with ray paths traversing the North SLLF and the central and southern segments of the ELLF, which may indicate narrower and less developed fault zones relative to the northern
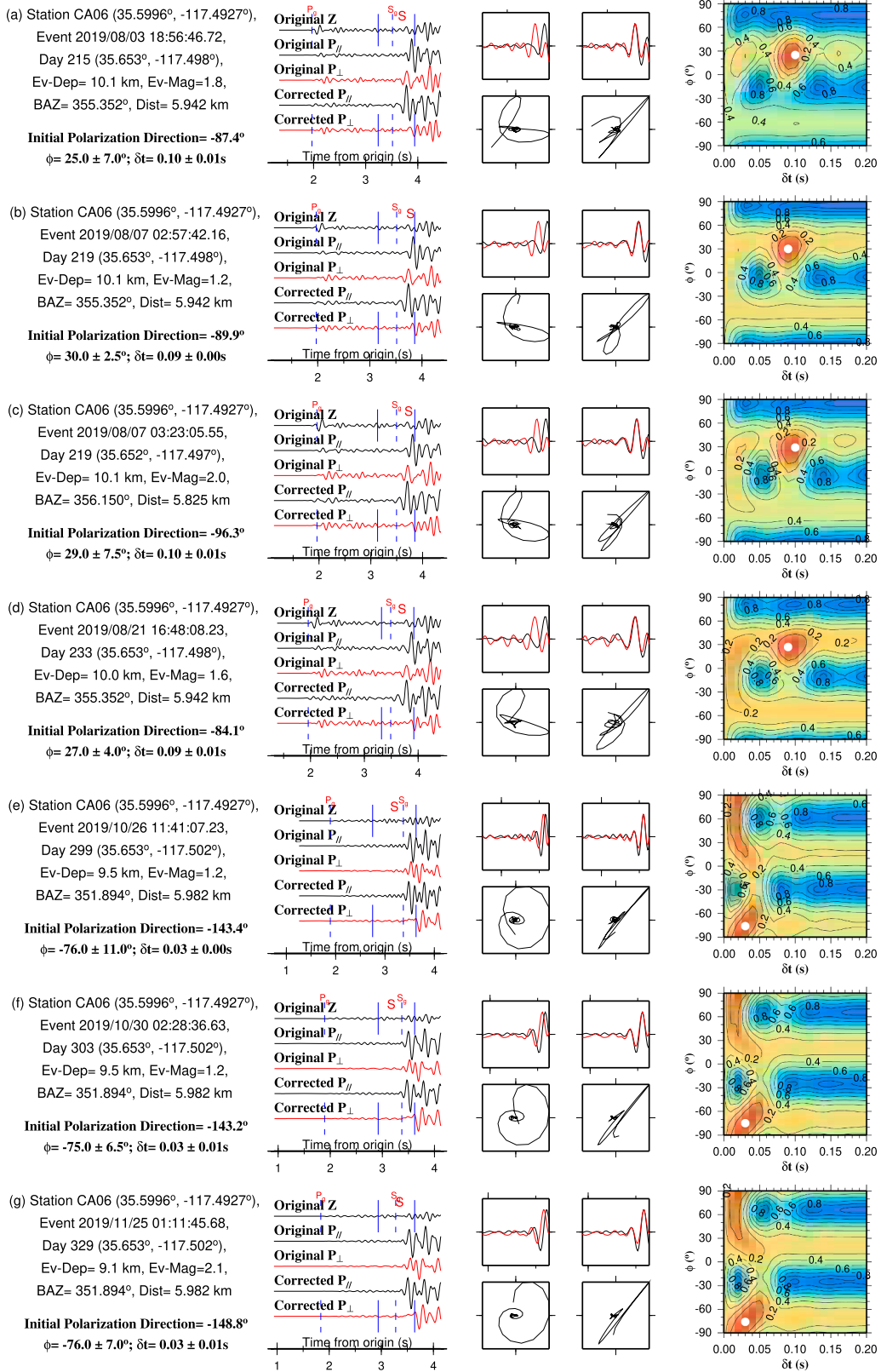
**Fig. 6.** Measurements from 7 events in the black circle in Fig. 3c that show apparent temporal variations. For each row, in the second column, the plots in the top row show the original vertical component and original and corrected initial polarization parallel ($P_{//}$) and initial polarization perpendicular ($P\perp$) components, and the plots in the third column show the uncorrected and corrected particle motions of the fast and slow particles. Note the $P_{//}$ and $P\perp$ components here are related to the initial polarization direction. The fourth column plots are corrected $P\perp$ energy contour maps, with the color representing the energy on the corrected $P\perp$ component. The optimal pair of splitting parameters correspond to the minimum value on the contour map of the remaining $P\perp$ component energy and are indicated by a white dot.

part of the ELLF. A clear temporal variation of anisotropy is observed near the intersection between the ELLF and the Cross-South-North blind fault and may indicate healing of NE-SW oriented fractures reactivated by the 2019 earthquake sequence.

## CRediT authorship contribution statement

**Yan Jia:** Data curation, Formal analysis, Funding acquisition, Investigation, Visualization, Writing – original draft, Writing – review & editing. **Stephen S. Gao:** Conceptualization, Funding acquisition, Methodology, Project administration, Resources, Software, Supervision, Validation, Writing – review & editing. **Kelly H. Liu:** Conceptualization, Funding acquisition, Methodology, Project administration, Resources, Software, Supervision, Validation, Writing – review & editing.

## Declaration of competing interest

The authors declare no conflicts of interest.

*Data Availability*

Seismic data from Stations CA01, CA03, CA06, and B921used in this study are publicly available from the SAGE (Seismological Facility for the Advancement of Geoscience) Data Management Center (https://ds.iris.edu/ds/nodes/dmc), and that from Station SV01 and the catalog of the relocated hypocenters were obtained from the California Earthquake Data Center (https://scedc.caltech.edu/). The Quaternary fault database of the United States was downloaded from the USGS (https://www.usgs.gov/programs/earthquake-hazards/faults). The shear wave splitting data has been shared as a link in the main text.

## Supplementary materials

Supplementary material associated with this article can be found, in the online version, at doi:10.1016/j.epsl.2024.118920.

## References

Ando, M., Ishikawa, Y., Wada, H., 1980. S-wave anisotropy in the upper mantle under a volcanic area in Japan. Nature 286 (5768), 43–46. https://doi.org/10.1038/286043a0.

Aster, R.C., Shearer, P.M., Berger, J., 1990. Quantitative measurements of shear wave polarizations at the Anza Seismic Network, southern California: implications for shear wave splitting and earthquake prediction. J. Geophys. Res. 95 (B8), 12449–12473. https://doi.org/10.1029/JB095iB08p12449.

Audet, P., 2015. Layered crustal anisotropy around the san andreas fault near parkfield, california. J. Geophys. Res., Solid Earth 120 (5), 3527–3543. https://doi.org/10.1002/2014JB011821.

Baccheschi, P., Pastori, M., Margheriti, L., Piccinini, D., 2016. Shear wave splitting of the 2009 L'Aquila seismic sequence: fluid saturated microcracks and crustal fractures in the Abruzzi region (Central Apennines, Italy). Geophys. J. Int. 204 (3), 1531–1549. https://doi.org/10.1093/gji/ggv536.

Barnhart, W.D., Hayes, G.P., Gold, R.D., 2019. The July 2019 Ridgecrest, California, earthquake sequence: kinematics of slip and stressing in cross-fault ruptures. Geophys. Res. Lett. 46 (21), 11859–11867. https://doi.org/10.1029/2019GL084741.

Bastow, I.D., Pilidou, S., Kendall, J.-M., Stuart, G.W., 2010. Melt-induced seismic anisotropy and magma assisted rifting in Ethiopia: evidence from surface waves. Geochem. Geophys. Geosyst. 11 (6), 2010GC003036 https://doi.org/10.1029/2010GC003036.

Bokelmann, G.H.R., Harjes, H., 2000. Evidence for temporal variation of seismic velocity within the upper continental crust. J. Geophys. Res. 105, 23879–23894. https://doi.org/10.1029/2000JB900207.

Boness, N.L., Zoback, M.D., 2004. Stress-induced seismic velocity anisotropy and physical properties in the SAFOD Pilot Hole in Parkfield, CA. Geophys. Res. Lett. 31, 2003GL019020 https://doi.org/10.1029/2003GL019020.

Boness, N.L., Zoback, M.D., 2006. Mapping stress and structurally controlled crustal shear velocity anisotropy in California. Geology 34 (10), 825–828. https://doi.org/10.1130/G22309.1.

Booth, D.C., Crampin, S., 1985. Shear-wave polarizations on a curved wavefront at an isotropic free surface. Geophys. J. Int. 83 (1), 31–45. https://doi.org/10.1111/j.1365-246X.1985.tb05154.x.

Brocher, T.M., Christensen, N.I., 1990. Seismic anisotropy due to preferred mineral orientation observed in shallow crustal rocks in southern Alaska. Geology 18 (8), 737–740. https://doi.org/10.1130/0091-7613(1990)018<0737:SADTPM>2.3.CO;2.

Cochran, E.S., Vidale, J.E., Li, Y., 2003. Near-fault anisotropy following the Hector Mine earthquake. J. Geophys. Res. 108 (B9), 2002JB002352 https://doi.org/10.1029/2002JB002352.

Cochran, E.S., Wolin, E., McNamara, D.E., Yong, A., Wilson, D., Alvarez, M., Van Der Elst, N., McClain, A., Steidl, J., 2020. The U.S. geological survey's rapid seismic array deployment for the 2019 Ridgecrest earthquake sequence. Seismol. Res. Lett. 91 (4), 1952–1960. https://doi.org/10.1785/0220190296.

Crampin, S., 1978. Seismic-wave propagation through a cracked solid: polarization as a possible dilatancy diagnostic. Geophys. J. Int. 53 (3), 467–496. https://doi.org/10.1111/j.1365-246X.1978.tb03754.x.

Crampin, S., 1991. Wave propagation through fluid-filled inclusions of various shapes: interpretation of extensive-dilatancy anisotropy. Geophys. J. Int. 104, 611–623. https://doi.org/10.1111/j.1365-246X.1991.tb05705.x.

Crampin, S., 1994. The fracture criticality of crustal rocks. Geophys. J. Int. 118 (2), 428–438. https://doi.org/10.1111/j.1365-246X.1994.tb03974.x.

Duan, H., Chu, Z., Zhang, S., Yang, C., Chen, J., Lei, J., 2022. Analysis of coseismic slip distributions and stress variations of the 2019 Mw 6.4 and 7.1 earthquakes in Ridgecrest, California. Tectonophysics 831, 229343. https://doi.org/10.1016/j.tecto.2022.229343.

DuRoss, C.B., Gold, R.D., Dawson, T.E., Scharer, K.M., Kendrick, K.J., Akciz, S.O., Angster, S.J., Bachhuber, J., Bacon, S., et al., 2020. Surface displacement distributions for the July 2019 Ridgecrest, California, earthquake ruptures. Bull. Seismol. Soc. Am. 110 (4), 1400–1418. https://doi.org/10.1785/0120200058.

Fialko, Y., Jin, Z., 2021. Simple shear origin of the cross-faults ruptured in the 2019 Ridgecrest earthquake sequence. Nat. Geosci. 14 (7), 513–518. https://doi.org/10.1038/s41561-021-00758-5.

Fielding, E.J., Liu, Z., Stephenson, O.L., Zhong, M., Liang, C., Moore, A., Yun, S.-H., Simons, M., 2020. Surface deformation related to the 2019 Mw 7.1 and 6.4 Ridgecrest earthquakes in California from GPS, SAR interferometry, and SAR pixel offsets. Seismol. Res. Lett. 91 (4), 2035–2046. https://doi.org/10.1785/0220190302.

Gao, S., Davis, P.M., Liu, H., Slack, P.D., Rigor, A.W., Zorin, Y.A., Mordvinova, V.V., Kozhevnikov, V.M., Logatchev, N.A., 1997. SKS splitting beneath continental rift zones. J. Geophys. Res. 102 (B10), 22781–22797. https://doi.org/10.1029/97JB01858.

Gao, Y., Crampin, S., 2004. Observations of stress relaxation before earthquakes. Geophys. J. Int. 157 (2), 578–582. https://doi.org/10.1111/j.1365-246X.2004.02207.x.

Gao, Y., Wang, P., Zheng, S., Wang, M., Chen, Y., Zhou, H., 1998. Temporal changes in shear-wave splitting at an isolated swarm of small earthquakes in 1992 near Dongfang, Hainan Island, southern China. Geophys. J. Int. 135 (1), 102–112. https://doi.org/10.1046/j.1365-246X.1998.00606.x.

Hauksson, E., Yoon, C., Yu, E., Andrews, J.R., Alvarez, M., Bhadha, R., Thomas, V., 2020. Caltech/USGS Southern california seismic network (SCSN) and southern california earthquake data center (SCEDC): data availability for the 2019 Ridgecrest sequence. Seismol. Res. Lett. 91 (4), 1961–1970. https://doi.org/10.1785/0220190290.

Hiramatsu, Y., Honma, H., Saiga, A., Furumoto, M., Ooida, T., 2005. Seismological evidence on characteristic time of crack healing in the shallow crust. Geophys. Res. Lett. 32 (9), 2005GL022657 https://doi.org/10.1029/2005GL022657.

Jiang, E., Liu, K.H., Gao, Y., Fu, X., Gao, S.S., 2021. Spatial variations of upper crustal anisotropy along the San Jacinto fault zone in Southern California: constraints from shear wave splitting analysis. J. Geophys. Res., Solid Earth 126 (4), e2020JB020876. https://doi.org/10.1029/2020JB020876.

Keir, D., Kendall, J., Ebinger, C.J., Stuart, G.W., 2005. Variations in late syn-rift melt alignment inferred from shear-wave splitting in crustal earthquakes beneath the Ethiopian rift. Geophys. Res. Lett. 32 (23), 2005GL024150 https://doi.org/10.1029/2005GL024150.

Kennett, B.L.N., Engdahl, E.R., 1991. iasp91 velocity model. doi: 10.17611/DP/9991809.

Leary, P.C., Crampin, S., McEvilly, T.V., 1990. Seismic fracture anisotropy in the Earth's crust: an overview. J. Geophys. Res. 95 (B7), 11105–11114. https://doi.org/10.1029/JB095iB07p11105.

Li, T., Gu, Y.J., Wang, Z., Wang, Ruijia, Chen, Y., Song, T.A., Wang, Ruihe, 2019. Spatiotemporal variations in crustal seismic anisotropy surrounding induced earthquakes near Fox Creek. Alberta. Geophys. Res. Lett. 46, 5180–5189. https://doi.org/10.1029/2018GL081766.

Li, Z., Peng, Z., 2017. Stress- and structure-induced anisotropy in Southern California from two decades of shear wave splitting measurements. Geophys. Res. Lett. 44 (19), 9607–9614. https://doi.org/10.1002/2017GL075163.

Li, Z., Zhang, H., Peng, Z., 2014. Structure-controlled seismic anisotropy along the Karadere–Düzce branch of the North Anatolian Fault revealed by shear-wave splitting tomography. Earth Planet. Sci. Lett. 391, 319–326. https://doi.org/10.1016/j.epsl.2014.01.046.

Liu, K.H., Gao, S.S., 2013. Making reliable shear-wave splitting measurements. Bull. Seismol. Soc. Am. 103 (5), 2680–2693. https://doi.org/10.1785/0120120355.

Liu, K.H., Gao, S.S., Gao, Y., Wu, J., 2008a. Shear wave splitting and mantle flow associated with the deflected Pacific slab beneath northeast Asia. J. Geophys. Res. 113 (B1), 2007JB005178 https://doi.org/10.1029/2007JB005178.

Liu, Y., Crampin, S., Main, I., 1997. Shear-wave anisotropy: spatial and temporal variations in time delays at Parkfield, Central California. Geophys. J. Int. 130 (3), 771–785. https://doi.org/10.1111/j.1365-246X.1997.tb01872.x.

Liu, Y., Teng, T.L., Ben-Zion, Y., 2004. Systematic analysis of shear-wave splitting in the aftershock zone of the 1999 Chi-Chi, Taiwan, earthquake: shallow crustal anisotropy and lack of precursory variations. Bull. Seismol. Soc. Am. 94 (6), 2330–2347. https://doi.org/10.1785/0120030139.

Liu, Y., Zhang, H., Kendall, J.M., Wookey, J., 2021. Conjugate fault deformation revealed by aftershocks of the 2013 Mw6.6 Lushan earthquake and seismic anisotropy tomography. Geophys. Res. Lett. 48, e2021GL092563 https://doi.org/10.1029/2021GL092563.

Liu, Y., Zhang, H., Thurber, C., Roecker, S., 2008b. Shear wave anisotropy in the crust around the san andreas fault near parkfield: spatial and temporal analysis. Geophys. J. Int. 172 (3), 957–970. https://doi.org/10.1111/j.1365-246X.2007.03618.x.

Miller, V., Savage, M., 2001. Changes in seismic anisotropy after volcanic eruptions: evidence from Mount Ruapehu. Science 293 (5538), 2231–2233. https://doi.org/10.1126/science.1063463.

Nuttli, O., 1961. The effect of the earth's surface on the S wave particle motion. Bull. Seismol. Soc. Am. 51 (2), 237–246. https://doi.org/10.1785/BSSA0510020237.

Pastori, M., Baccheschi, P., Margheriti, L., 2019. Shear wave splitting evidence and relations with stress field and major faults from the "Amatrice-Visso-Norcia Seismic Sequence. Tectonics 38 (9), 3351–3372. https://doi.org/10.1029/2018TC005478.

Peng, Z., Ben-Zion, Y., 2004. Systematic analysis of crustal anisotropy along the karadere-düzce branch of the north anatolian fault. Geophys. J. Int. 159, 253–274. https://doi.org/10.1111/j.1365-246X.2004.02379.x.

Plesch, A., Shaw, J.H., Ross, Z.E., Hauksson, E., 2020. Detailed 3D fault representations for the 2019 Ridgecrest, California, earthquake sequence. Bull. Seismol. Soc. Am. 110 (4), 1818–1831. https://doi.org/10.1785/0120200053.

Ponti, D.J., Blair, J.L., Rosa, C.M., Thomas, K., Pickering, A.J., Akciz, S., Angster, S., Avouac, J.-P., et al., 2020. Documentation of surface fault rupture and ground-deformation features produced by the 4 and 5 July 2019 Mw 6.4 and Mw 7.1 Ridgecrest earthquake sequence. Seismol. Res. Lett. 91 (5), 2942–2959. https://doi.org/10.1785/0220190322.

Ross, Z.E., Idini, B., Jia, Z., Stephenson, O.L., Zhong, M., Wang, X., Zhan, Z., Simons, M., Fielding, E.J., Yun, S.-H., Hauksson, E., Moore, A.W., Liu, Z., Jung, J., 2019.

Hierarchical interlocked orthogonal faulting in the 2019 Ridgecrest earthquake sequence. Science 366 (6463), 346–351. https://doi.org/10.1126/science.aaz0109.

Sayers, C.M., 1994. The elastic anisotropy of shales. J. Geophys. Res. 99 (B1), 767–774. https://doi.org/10.1029/93JB02579.

Shelly, D.R., 2020. A high-resolution seismic catalog for the initial 2019 Ridgecrest earthquake sequence: foreshocks, aftershocks, and faulting complexity. Seismol. Res. Lett. 91 (4), 1971–1978. https://doi.org/10.1785/0220190309.

Sheng, S., Meng, L., 2020. Stress field variation during the 2019 Ridgecrest earthquake sequence. Geophys. Res. Lett. 47 (15), e2020GL087722 https://doi.org/10.1029/2020GL087722.

Shi, Y., Gao, Y., Shen, X., Liu, K.H., 2020. Multiscale spatial distribution of crustal seismic anisotropy beneath the northeastern margin of the Tibetan plateau and tectonic implications of the Haiyuan fault. Tectonophysics 774, 228274. https://doi.org/10.1016/j.tecto.2019.228274.

Silver, P.G., Chan, W.W., 1991. Shear wave splitting and subcontinental mantle deformation. J. Geophys. Res. 96 (B10), 16429–16454. https://doi.org/10.1029/91JB00899.

Smith, W.H., Wessel, P., 1990. Gridding with continuous curvature splines in tension. Geophysics 55 (3), 293–305.

Tadokoro, K., Ando, M., 2002. Evidence for rapid fault healing derived from temporal changes in S wave splitting. Geophys. Res. Lett. 29 (4), 6–10. https://doi.org/10.1029/2001GL013644.

Volti, T., Crampin, S., 2003. A four-year study of shear-wave splitting in Iceland: 2. Temporal changes before earthquakes and volcanic eruptions. Geological Society, London. Special Publications 212 (1), 135–149. https://doi.org/10.1144/GSL.SP.2003.212.01.09.

Walsh, E., Arnold, R., Savage, M.K., 2013. Silver and chan revisited. J. Geophys. Res. 118 (10), 5500–5515. https://doi.org/10.1002/jgrb.50386.

White, M.C.A., Fang, H., Catchings, R.D., Goldman, M.R., Steidl, J.H., Ben-Zion, Y., 2021. Detailed traveltime tomography and seismic catalogue around the 2019 M w7.1 Ridgecrest, California, earthquake using dense rapid-response seismic data. Geophys. J. Int. 227 (1), 204–227. https://doi.org/10.1093/gji/ggab224.

Wills, C.J., 1988. Little lake and airport lake fault zones. california, california division of mines and geology fault evaluation report FER-199.

Woodcock, N.H., Fischer, M., 1986. Strike-slip duplexes. J. Struct. Geol. 8 (7), 725–735. https://doi.org/10.1016/0191-8141(86)90021-0.

Yue, H., Sun, J., Wang, M., Shen, Z., Li, M., Xue, L., Lu, W., Zhou, Y., Ren, C., Lay, T., 2021. The 2019 Ridgecrest, California earthquake sequence: evolution of seismic and aseismic slip on an orthogonal fault system. Earth Planet. Sci. Lett. 570, 117066 https://doi.org/10.1016/j.epsl.2021.117066.

Zhang, Z., Schwartz, S.Y., 1994. Seismic anisotropy in the shallow crust of the loma prieta segment of the san andreas fault system. J. Geophys. Res. 99 (B5), 9651–9661. https://doi.org/10.1029/94JB00241.

Zinke, J.C., Zoback, M.D., 2000. Structure-related and stress-induced shear-wave velocity anisotropy: observations from microearthquakes near the Calaveras Fault in central California. Bull. Seismol. Soc. Am. 90 (5), 1305–1312. https://doi.org/10.1785/0119990099.